

Supplementary Information for "GUIDe: Generative and Uncertainty-Informed Inverse Design for On-Demand Nonlinear Functional Responses"

Haoxuan Dylan Mu¹, Mingjian Tang¹, Wei Gao^{1,2}, and Wei “Wayne” Chen¹

¹*J. Mike Walker '66 Department of Mechanical Engineering, Texas A&M University, College Station, United States*

²*Department of Materials Science & Engineering, Texas A&M University, College Station, United States*

1 Background on nacre-inspired material

Biological material shows exceptional mechanical properties governed by its highly controlled hierarchical features, incorporating minerals into soft matrices. While the structural property of hard biological materials generally falls short compared to engineering materials like steels or fibre-reinforced composites, these natural composites demonstrate enhanced mechanical performance relative to those of their constituent phases, namely brittle minerals and weak proteins¹. Specifically, biological materials achieve a synergy of toughness, strength, stiffness, and lightweight that is unparalleled in engineering materials.

Nacre, a natural composite found in the inner shell of molluscs, is an excellent example of such high-performance biological materials. Constituted by 95 wt% of a ceramic phase, hard and brittle mineral tablets (calcite, aragonite), bonded with 5 wt% thin, viscoelastic, and resilient organic interface that encases the ceramic phase^{2–4}, nacre materials are formed as brick-and-mortar structures. Despite of the minimal composition, the organic matrix plays a significant role in the toughening mechanisms, and contributes to the energy dissipation of the nacre system on meso-, micro-, and nano-levels, including crack path deflection^{5–7}, creation of new surface through multiple microcracking⁸, crack bridging by the organic ligaments⁹, unfolding of cross-links¹⁰. With these interface toughening mechanisms, the nacre material can achieve a toughness thousands of times higher than that of its monolithic constituent, yet without significantly sacrificing strength or stiffness^{3, 11, 12}.

Inspired by nacre, studies have been done to harness the superior mechanical properties induced by the unique structure in applications of impact-resistance materials^{13–20} and biomedical implants^{21–29}. With the development of flexible nanocomposites, nacre-inspired thin films was proven to exhibit both excellent mechanical properties and conductivity, and therefore intriguing a growing demand for its application in flexible electronics^{30–38}, where tailoring nacre-inspired material through interface properties, typically exhibiting strong nonlinearity, following particular stress-strain behavior is crucially needed.

2 Genetic algorithm baseline

We benchmark inverse design with a genetic algorithm that minimizes the mean-squared error between the predicted response and the target:

$$\min_{\mathbf{x} \in \mathbb{R}^d} \frac{1}{L} \|\hat{\mathbf{y}}(\mathbf{x}) - \mathbf{y}^*\|_2^2. \quad (1)$$

To ensure constraint satisfaction, we apply a 10^{16} penalty to individuals that do not follow $\Delta\sigma_n^1/\Delta\delta_n^1 < \sigma_n^y/\delta_n^y$ and $\Delta\sigma_s^1/\Delta\delta_s^1 < \sigma_s^y/\delta_s^y$. The range of the search space is set from zero to seven times the standard deviation of the data distribution. For in-distribution targets, we evaluate the quality of a small set of generated designs in a fast-generation run. To keep a fair computational budget for benchmarking, we use a population size of 100, 10 generations (i.e., 1,000 evaluations). In each generation, 30 parents are selected via tournament; offspring are produced by uniform crossover; mutation perturbs 30% of genes by adding zero-mean Gaussian noise with standard deviation equal to 5% of the search space. Elitism retains the top 5 individuals. This configuration provides moderate selection pressure while preserving diversity; the relatively high mutation rate compensates for the shallow run. We report the best 50 candidates pooled across all generations.

For out-of-distribution targets, we increase exploration to deal with more challenging landscapes. Particularly, we increase the population size and the number of generations to 200 and 400, respectively, and strengthen elitism by retaining the top 30 individuals. Other configurations are kept the same. We summarize the settings and parameters for GA in Table 1.

Table 1. GA settings for in-distribution (ID) and out-of-distribution (OOD) targets.

Setting	ID targets	OOD targets
Population size	100	200
Generations	10	400
Evaluations (pop \times gen)	1,000	80,000
Parents per generation	30	30
Parent selection	Tournament	Tournament
Crossover	Uniform	Uniform
Mutation rate	30%	30%
Elitism (kept parents)	5	30
Reporting	Top 50 overall candidates	Top 200 overall candidates
Objective	Minimize MSE	Minimize MSE

3 Conditional 1D UNet baseline

Here we provide implementation details and parameters for the denoising diffusion baseline discussed in the main text. A summary of the setting is provided in Table 2.

Table 2. Key conditional 1D UNet diffusion settings.

Setting	Value
Backbone	1D UNet, depth $D=3$; one DOUBLECONV per stage
Normalization	GroupNorm ($G=8$)
Activation	SiLU
Feature-map lengths (down path)	$100 \rightarrow 50 \rightarrow 25 \rightarrow 13$
Channels per scale	$64 \rightarrow 128 \rightarrow 256 \rightarrow 512$
Attention	Pre-norm MHA (4 heads); bottleneck spatial self-attention; per-block 1D CBAM after DOUBLECONV.
Conditioning	FiLM
Time encoding	Sinusoidal
Timesteps	$T=1,000$
Noise schedule	Linear $\beta_t \in [10^{-4}, 0.02]$
Batch size	64
Optimizer	AdamW
learning rate	3×10^{-4}
Dropout	$p=0.1$ (bottleneck and time embedding)
Iterations	2,500; early stopping (patience 200)

3.1 Forward diffusion, noise schedule, and objective

We consider a conditional denoising diffusion probabilistic model (DDPM)³⁹ for inverse design, where the goal is to generate a design vector $\mathbf{x}_0 \in \mathbb{R}^d$ given a target response curve $\mathbf{y}^* \in \mathbb{R}^L$. A T -step forward noising process produces $\{\mathbf{x}_t\}_{t=0}^T$ via

$$\beta_t \in (0, 1), \quad \alpha_t = 1 - \beta_t, \quad \bar{\alpha}_t = \prod_{s=0}^t \alpha_s, \quad (2)$$

$$q(\mathbf{x}_t | \mathbf{x}_0) = \mathcal{N}(\mathbf{x}_t; \sqrt{\bar{\alpha}_t} \mathbf{x}_0, (1 - \bar{\alpha}_t) \mathbf{I}). \quad (3)$$

At training time a neural network ϵ_θ predicts the Gaussian noise ϵ from a noisy input \mathbf{x}_t , the timestep t , and the condition \mathbf{y}^* :

$$\epsilon_\theta : \mathbb{R}^d \times \{0, \dots, T-1\} \times \mathbb{R}^L \rightarrow \mathbb{R}^d. \quad (4)$$

We use a linear schedule $\beta_t = \text{linspace}(10^{-4}, 0.02, T)$, with $T = 1,000$, hence $\alpha_t = 1 - \beta_t$ and $\bar{\alpha}_t$ as above. As a simplified form of optimizing the variational lower bound of log-likelihood, the standard DDPM training objective follows the MSE between the true noise and the prediction:

$$\mathcal{L}(\theta) = \mathbb{E}_{\mathbf{x}_0, \mathbf{y}^*, t, \epsilon} \left[\|\epsilon - \epsilon_\theta(\mathbf{x}_t, t, \mathbf{y}^*)\|_2^2 \right], \quad \mathbf{x}_t = \sqrt{\alpha_t} \mathbf{x}_0 + \sqrt{1 - \bar{\alpha}_t} \epsilon, \quad \epsilon \sim \mathcal{N}(0, \mathbf{I}). \quad (5)$$

3.2 Time and condition embeddings

Discrete timesteps t are mapped to a vector $\gamma(t) \in \mathbb{R}^{D_t}$ by a sinusoidal embedding

$$\gamma(t) = [\sin(\omega_1 t), \cos(\omega_1 t), \dots, \sin(\omega_{D_t}/2 t), \cos(\omega_{D_t}/2 t)], \quad \omega_k = \frac{1}{10000^{(2k-2)/D_t}}, \quad (6)$$

with $D_t=128$. The curve $\mathbf{y}^* \in \mathbb{R}^L$ is mapped to a global vector $\phi(\mathbf{y}^*) \in \mathbb{R}^{D_t}$ via a linear layer and SiLU. The global conditioning vector is the concatenation

$$c = [\gamma(t); \phi(\mathbf{y}^*)] \in \mathbb{R}^{2D_t} = \mathbb{R}^{256}. \quad (7)$$

To align the spatial dimension of the UNet with the curve domain, we build an L -length feature map (in our material design problem, $L = 100$). First, a 1D convolution produces $f_y(\mathbf{y}^*) \in \mathbb{R}^{C_0 \times L}$ with $C_0 = 64$. Then the noisy design vector $\mathbf{x}_t \in \mathbb{R}^d$ is projected to length L by a linear map $W_x \in \mathbb{R}^{L \times d}$, yielding $u = W_x \mathbf{x}_t \in \mathbb{R}^L$. We broadcast u across channels and add it to $f_y(\mathbf{y}^*)$ to form the initial tensor

$$H^{(0)} = f_y(\mathbf{y}^*) + \text{Broadcast}(u) \in \mathbb{R}^{C_0 \times L}. \quad (8)$$

This design enforces a pointwise correspondence between the spatial grid of \mathbf{y} and all subsequent convolutions.

3.3 Building blocks

We use GroupNorm⁴⁰ ($G=8$) and SiLU⁴¹ in all convolutions, with dropout $p=0.1$ applied to the bottleneck and the time embedding. Each convolutional block is modulated by feature-wise linear modulation (FiLM)⁴² driven by the global condition c : we compute affine parameters via a linear map and apply them channel-wise along the length dimension,

$$\begin{aligned} (\gamma_c, \beta_c) &= W_{\text{FiLM}} c \in \mathbb{R}^{2C}, \\ \text{FiLM}(X, c) &= X \odot (1 + \gamma_c) + \beta_c, \quad X \in \mathbb{R}^{C \times L}, \end{aligned} \quad (9)$$

with (γ_c, β_c) broadcast over L . A DOUBLECONV unit stacks two 3×1 convolutions, each followed by GN→SiLU→FiLM, then applies the convolutional block attention module (CBAM)⁴³ to reweight channels and positions. At each resolution, we apply multi-head self-attention along the length axis by viewing $H \in \mathbb{R}^{C \times L}$ as L tokens ($H^\top \in \mathbb{R}^{L \times C}$), using pre-norm MHA and a lightly scaled residual,

$$H \leftarrow H + \lambda \hat{H}, \quad \lambda = 0.1, \quad (10)$$

where \hat{H} is the attention output with four heads. In the bottleneck, we use a single-head dot-product attention over L with 1×1 projections for queries/keys/values, followed by a residual projection:

$$\begin{aligned} q, k, v &= \text{Conv1d}_{1 \times 1}(H), \quad A = \text{softmax}\left(\frac{q^\top k}{\sqrt{C}}\right) \in \mathbb{R}^{L \times L}, \\ H &\leftarrow \text{Conv1d}_{1 \times 1}(vA^\top) + H. \end{aligned} \quad (11)$$

CBAM is applied in two sequential steps. First, we aggregate features over the length dimension using global average pooling (GAP) and global max pooling (GMP), feed their sum to a two-layer MLP with SiLU, and pass the result through a sigmoid to obtain per-channel weights $s \in \mathbb{R}^C$; these weights are broadcast along L and used to reweight the channels of X . Second, we form a two-channel map by concatenating the channel-wise mean and max of the reweighted features, apply a 1D convolution (kernel size 7) followed by a sigmoid to produce a spatial mask $m \in \mathbb{R}^{1 \times L}$; this mask is broadcast across channels and multiplied with the feature map. The two masks are applied in order (channel then spatial) and preserve the original tensor shape.

3.4 UNet backbone

The 1D UNet follows a coarse-to-fine pathway that mirrors the structure of the target curve. Channels grow geometrically with scale, $C_i = 64 \cdot 2^i$ for $i = 0, \dots, D$ and depth $D=3$, so that early layers capture local detail while deeper layers gather global context. The encoder begins with a DOUBLECONV at C_0 and then, for each level $i = 0 \dots D-1$, halves the length with a learned strided downsample (4×1 conv, stride 2), refines features with a DOUBLECONV at C_{i+1} , and applies multi-head self-attention along the length dimension to connect distant curve segments. Immediately before the deepest level, we cache the skip tensors—high-resolution descriptors that will later anchor reconstruction. At the bottleneck, a DOUBLECONV is followed by spatial self-attention, dropout, and another DOUBLECONV at width C_D , stitching together long-range dependencies while regularizing the representation. The decoder then inverts the process: for $i = D-1 \dots 0$ we upsample the features linearly by a factor of 2, concatenate the aligned skip from the encoder (yielding $C_{i+1} + C_i$ channels), and fuse with a 3×1 conv \rightarrow GN \rightarrow SiLU block before a DOUBLECONV at C_i and an attention layer. Finally, a 3×1 convolution compresses the width to a single channel over the curve length, and a final linear map $W_{\text{out}} \in \mathbb{R}^{d \times L}$ produces $\epsilon_\theta(\mathbf{x}_t, t, \mathbf{y}^*) = W_{\text{out}} h \in \mathbb{R}^d$.

3.5 Training and sampling protocols

We train the noise predictor ϵ_θ with the objective Eq. 5 on batches of size 64 (train/val/test sizes: 1,669/2,833/2,834). For each example we sample t and ϵ , corrupt the clean design x_0 , predict $\hat{\epsilon} = \epsilon_\theta(\mathbf{x}_t, t, \mathbf{y}^*)$, and minimize the mean-squared error, optimizing with AdamW⁴⁴ (learning rate 3×10^{-4}). Training proceeds for up to 2,500 epochs with early stopping based on the validation loss (patience 200 epochs without improvement); the best checkpoint (lowest validation loss) is saved and achieves a validation loss of 0.168 with 1,669 design–response training points. To stabilize conditioning at initialization, every FiLM linear layer is initialized with weights and biases drawn from $\mathcal{N}(0, 10^{-2})$, keeping early γ, β near zero. At inference, we generate x_0 by ancestral sampling starting at $x_T \sim \mathcal{N}(0, \mathbf{I})$ and stepping $t=T-1 \rightarrow 0$ via

$$x_{t-1} = \frac{1}{\sqrt{\alpha_t}} \left(x_t - \frac{\beta_t}{\sqrt{1 - \bar{\alpha}_t}} \epsilon_\theta(\mathbf{x}_t, t, \mathbf{y}^*) \right) + \mathbb{1}_{t>0} \sqrt{\beta_t} z_t, \quad z_t \sim \mathcal{N}(0, \mathbf{I}), \quad (12)$$

thereby producing a sample consistent with the target curve \mathbf{y}^* .

4 Likelihood visualization through a synthetic problem

To observe how the high-likelihood region in the design space matches the real feasible region, we designed a 2D trigonometric synthetic problem that shows multiple feasible regions in the design space. In this problem, the functional response is given by

$$f(x_1, x_2, s) = \sin(3\pi x_1 + s) + \cos(3\pi x_2), X = [-1, 1]^2, \quad (13)$$

where the model is learning the mapping and generating design parameters x_1, x_2 that yield response that matches the target. We plot the likelihood heatmap given the target being the response of design $(x_1, x_2) = (0, 0)$. Because of the periodicity of the function, design sets that are offset by integer multiples of the period yield the same response; consequently, we expect nine regularly located high-likelihood regions, highlighted in blue, within the design space. The dashed line delineate the boundary of the set of domain meeting the target, i.e., $\{(x_1, x_2) \in X \mid \forall s \in S, T(x_1, x_2, s) - \mathbf{y}^*(s) \leq \epsilon\}$. According to the figure, we can observe that the domain assigned with high likelihood score precisely overlaps with the target met domain, under varying tolerances. This explains how the method can recover multiple feasible regions and track their extent as tolerances vary.

5 Expanded results on ID cases

We here present the real stress–strain response obtained from FEM evaluation of generated feasible designs of GUIDe (Fig. 2a), denoising diffusion (Fig. 2b), and genetic algorithm (Fig. 2c), including the target curve and a tolerance equals to 10% of its target’s tensile strength. A set of six random responses was selected from the test dataset as targets (belonging to the 50 targets examined in Sec. 2.4.1 of the main article)

6 Expanded results on OOD Case 3 and 4

Here we show the full pairwise distribution of the feasible designs generated by GUIDe, CDM, and GA. As discussed in the results section of the main article, GUIDe results demonstrate its superiority in the number of feasible designs generated, diversity, and novelty.

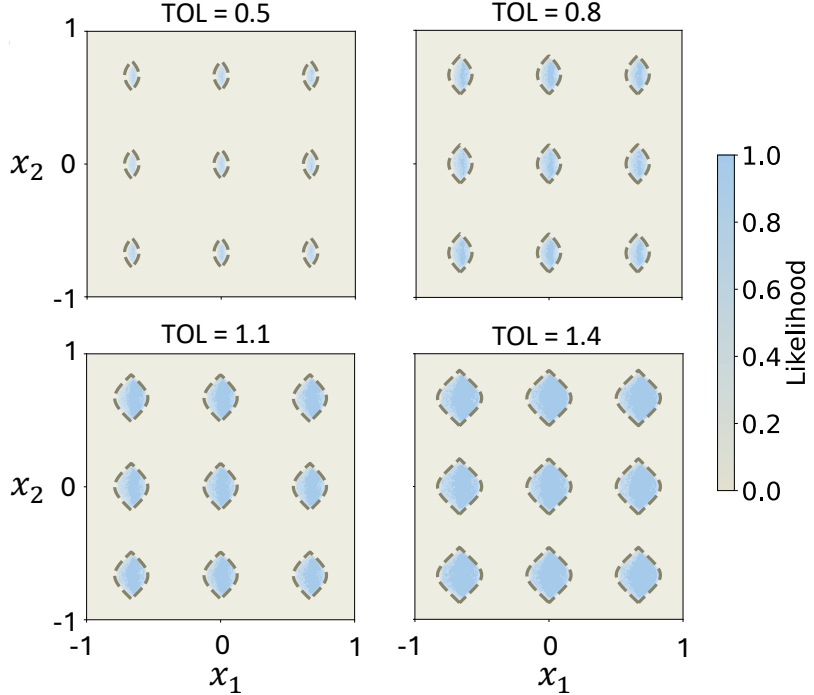


Figure 1. Evaluation of high-likelihood set coverage on a synthetic problem. Each panel shows a likelihood heatmap over the design space under different tolerance settings. Dashed boundaries mark the true feasible regions. Across tolerance levels, high-likelihood areas concentrate within the ground-truth feasible sets.

7 Expanded results on extreme OOD targets

To observe the reaction of the models to anomalous or physically unachievable conditions, as illustrated in Fig. 5, we formulated two synthetic stress-strain targets: a parabolic response defined as

$$\sigma_t(\varepsilon) = \begin{cases} -100\varepsilon^2 + 300\varepsilon, & \text{if } 0 \leq \varepsilon \leq 3 \\ 0, & \text{if } 3 < \varepsilon \leq 4, \end{cases} \quad (14)$$

and a Gaussian noise response, where

$$\sigma_t(\varepsilon) \sim \mathcal{N}(50, 100), \quad \varepsilon \in [0, 4]. \quad (15)$$

These two target curves are devised as representations that no existing designs are expected to match these responses; therefore, a “responsible” inverse generative algorithm should be able to identify such an anomaly. Following the same design generation and validation procedure as in other design cases, we selected 200 candidates from the 2,000 sampled designs, and then tested the tensile stress-strain response under FEM. We discussed in Sec. 2.4.2 of the main text that while GUIDe recognized the OOD and successfully refused to generate any samples, CDM generated misleading results. Here, we add a detailed description of the designs generated by the genetic algorithm. For the case of the Gaussian noise target, as shown in the left panel of Fig. 5a and b, GA’s results show a large prediction mismatch. However, by comparing the right panel of Fig. 5a and b, we discover that while top candidates from GA demonstrate a close prediction alignment given the target of the parabolic response, after FEM validation, none of the real stress-strain responses of these designs match the target. This result demonstrates that optimizing based on the forward model’s prediction without considering the uncertainty can lead to failure of OOD detection, thereby compromising the trustworthiness of the generative design framework.

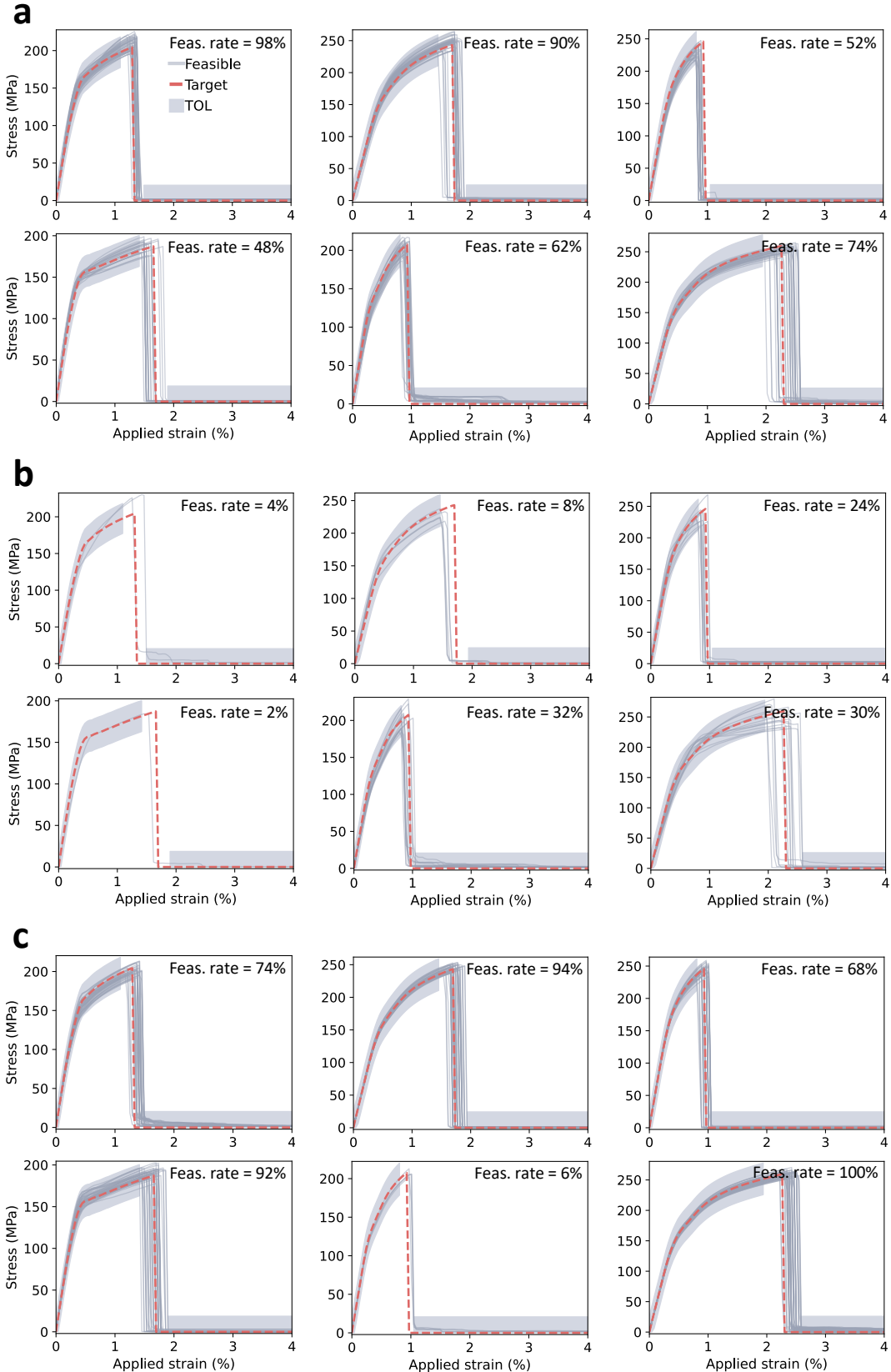


Figure 2. Evaluation of feasible designs' stress–strain curve from GUIDe, GA, and CDM conditioned on targets selected from the test dataset. The feasibility rate of each instance is denoted. The shown targets belong to the in-distribution study in the Sec. 2.4.1 of the main text. **a, b, c**, present the generation results by GUIDe, GA, and CDM, respectively.

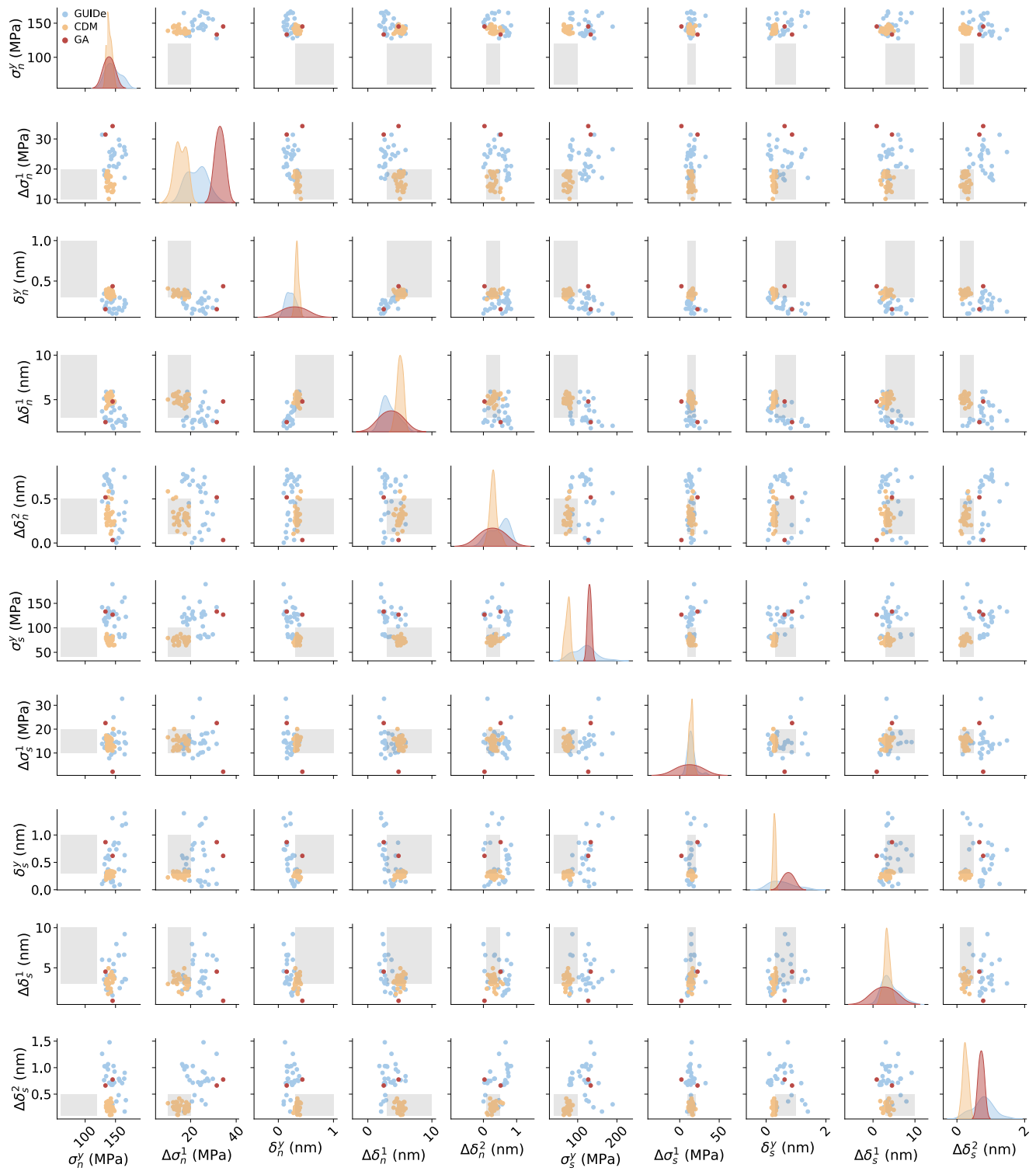


Figure 3. Distribution of feasible designs generated by GUIDe, CDM, and GA for Case 3

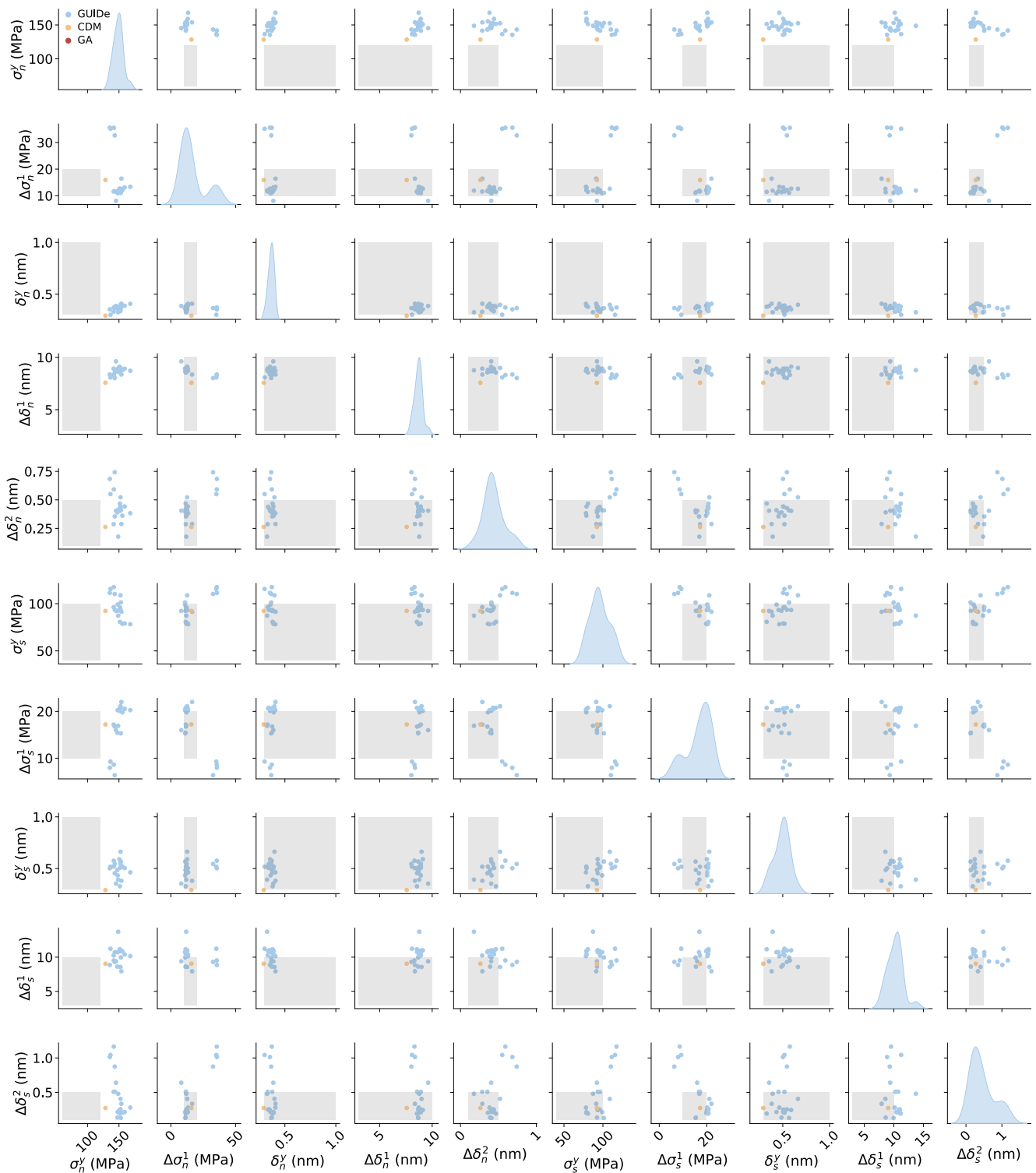


Figure 4. Distribution of feasible designs generated by GUIDe, CDM, and GA for Case 4

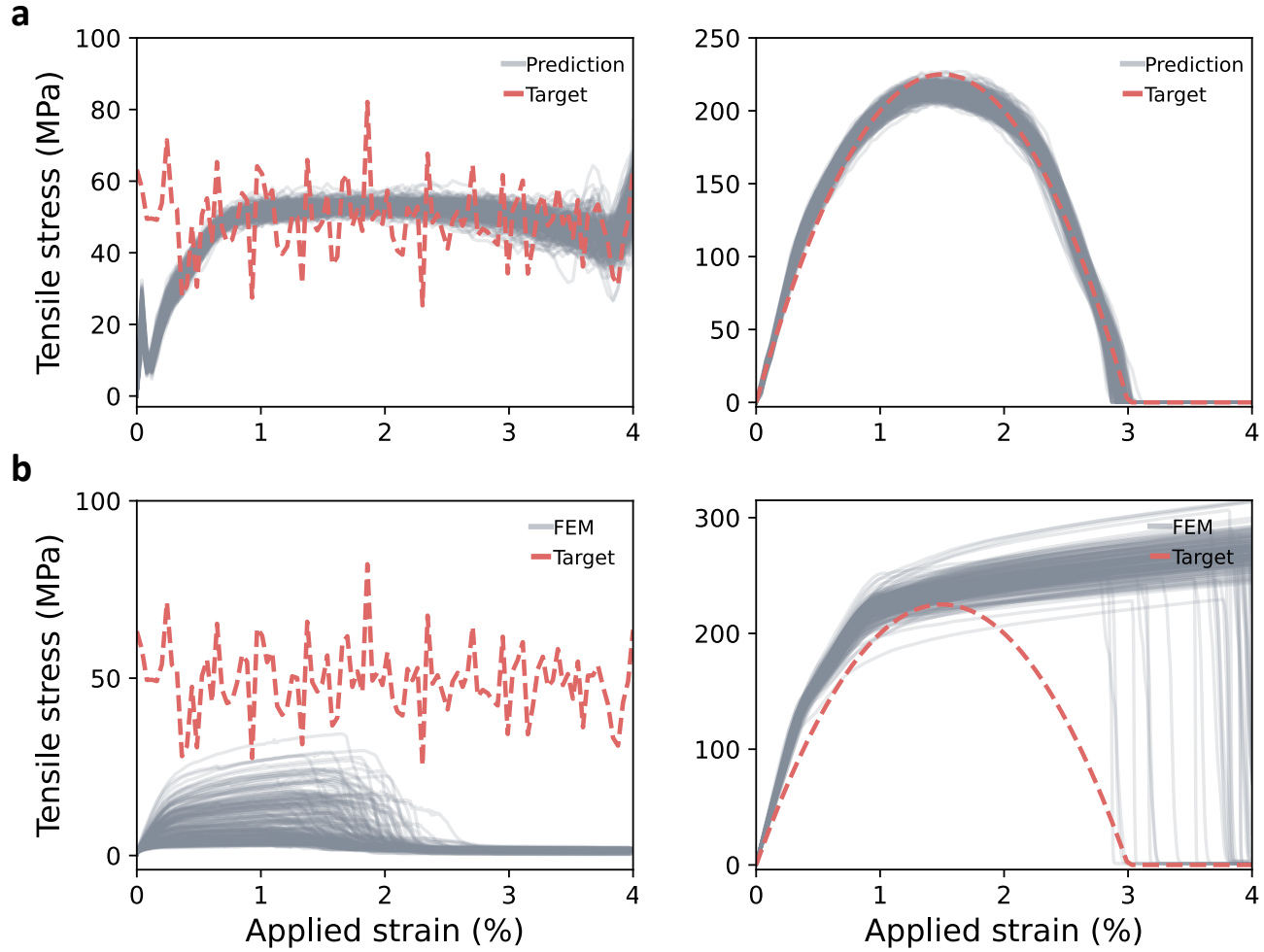


Figure 5. Evaluation of GA performance on extreme OOD targets. **a**, Without considering epistemic uncertainty, the predictive response of GA's generation seems close to the target. **b**, None of the real responses obtained through FEM are consistent with the prediction. This result indicates that GA can generate misleading results as well, without uncertainty information in the process of design generation.

References

1. Barthelat, F., Yin, Z. & Buehler, M. J. Structure and mechanics of interfaces in biological materials. *Nat. Rev. Mater.* **1**, 1–16 (2016).
2. Barthelat, F., Tang, H., Zavattieri, P. D., Li, C.-M. & Espinosa, H. D. On the mechanics of mother-of-pearl: a key feature in the material hierarchical structure. *J. Mech. Phys. Solids* **55**, 306–337 (2007).
3. Espinosa, H. D., Rim, J. E., Barthelat, F. & Buehler, M. J. Merger of structure and material in nacre and bone—perspectives on de novo biomimetic materials. *Prog. Mater. Sci.* **54**, 1059–1100 (2009).
4. Mayer, G. Rigid biological systems as models for synthetic composites. *Science* **310**, 1144–1147 (2005).
5. Bouville, F. *et al.* Strong, tough and stiff bioinspired ceramics from brittle constituents. *Nat. materials* **13**, 508–514 (2014).
6. Ritchie, R. O. The conflicts between strength and toughness. *Nat. materials* **10**, 817–822 (2011).
7. Gao, H.-L. *et al.* Mass production of bulk artificial nacre with excellent mechanical properties. *Nat. communications* **8**, 287 (2017).
8. Kamat, S., Su, X., Ballarini, R. & Heuer, A. Structural basis for the fracture toughness of the shell of the conch *strombus gigas*. *Nature* **405**, 1036–1040 (2000).
9. Ji, B. & Gao, H. Mechanical properties of nanostructure of biological materials. *J. Mech. Phys. Solids* **52**, 1963–1990 (2004).
10. Tang, Z., Kotov, N. A., Magonov, S. & Ozturk, B. Nanostructured artificial nacre. *Nat. materials* **2**, 413–418 (2003).
11. Barthelat, F. Nacre from mollusk shells: a model for high-performance structural materials. *Bioinspiration & biomimetics* **5**, 035001 (2010).
12. Corni, I. *et al.* A review of experimental techniques to produce a nacre-like structure. *Bioinspiration & biomimetics* **7**, 031001 (2012).
13. Amini, A., Khavari, A., Barthelat, F. & Ehrlicher, A. J. Centrifugation and index matching yield a strong and transparent bioinspired nacreous composite. *Science* **373**, 1229–1234 (2021).
14. Yin, Z., Hannard, F. & Barthelat, F. Impact-resistant nacre-like transparent materials. *Science* **364**, 1260–1263 (2019).
15. Zhang, X., Wu, K., Ni, Y. & He, L. Anomalous inapplicability of nacre-like architectures as impact-resistant templates in a wide range of impact velocities. *Nat. Commun.* **13**, 7719 (2022).
16. Gu, G. X., Takaffoli, M. & Buehler, M. J. Hierarchically enhanced impact resistance of bioinspired composites. *Adv. Mater.* **29**, 1700060 (2017).
17. Gu, G. X., Takaffoli, M., Hsieh, A. J. & Buehler, M. J. Biomimetic additive manufactured polymer composites for improved impact resistance. *Extrem. Mech. Lett.* **9**, 317–323 (2016).
18. Ko, K., Jin, S., Lee, S. E. & Hong, J.-W. Impact resistance of nacre-like composites diversely patterned by 3d printing. *Compos. Struct.* **238**, 111951 (2020).
19. Pan, H. *et al.* Hierarchical toughening of a biomimetic bulk cement composite. *ACS Appl. Mater. & Interfaces* **12**, 53297–53309 (2020).
20. Miao, T. *et al.* Ballistic performance of bioinspired nacre-like aluminium composite plates. *Compos. Part B: Eng.* **177**, 107382 (2019).
21. Tang, Z., Wang, Y., Podsiadlo, P. & Kotov, N. A. Biomedical applications of layer-by-layer assembly: from biomimetics to tissue engineering. *Adv. materials* **18**, 3203–3224 (2006).
22. Costa, R. R. & Mano, J. F. Polyelectrolyte multilayered assemblies in biomedical technologies. *Chem. Soc. Rev.* **43**, 3453–3479 (2014).
23. Le Ferrand, H., Goh, B. T. & Teoh, S.-H. Nacre-like ceramic composites: Properties, functions and fabrication in the context of dental restorations. *Acta Biomater.* **173**, 66–79 (2024).
24. Rodrigues, J. R., Alves, N. M. & Mano, J. F. Nacre-inspired nanocomposites produced using layer-by-layer assembly: Design strategies and biomedical applications. *Mater. Sci. Eng. C* **76**, 1263–1273 (2017).

25. Han, J. *et al.* Biomimetic design and assembly of organic–inorganic composite films with simultaneously enhanced strength and toughness. *Chem. Commun.* **47**, 5274–5276 (2011).
26. Zhang, G. *et al.* Nacre, a natural, multi-use, and timely biomaterial for bone graft substitution. *J. Biomed. Mater. Res. Part A* **105**, 662–671 (2017).
27. Couto, D. S., Alves, N. M. & Mano, J. F. Nanostructured multilayer coatings combining chitosan with bioactive glass nanoparticles. *J. nanoscience nanotechnology* **9**, 1741–1748 (2009).
28. Patel, I. F., Kiryukhin, M. V., Yakovlev, N. L., Gupta, H. S. & Sukhorukov, G. B. Naturally inspired polyelectrolyte multilayer composite films synthesised through layer-by-layer assembly and chemically infiltrated with caco 3. *J. Mater. Chem. B* **3**, 4821–4830 (2015).
29. Gil, S., Silva, J. M. & Mano, J. F. Magnetically multilayer polysaccharide membranes for biomedical applications. *ACS Biomater. Sci. & Eng.* **1**, 1016–1025 (2015).
30. Wang, L. *et al.* Flexible multiresponse-actuated nacre-like mxene nanocomposite for wearable human-machine interfacing. *Matter* **5**, 3417–3431 (2022).
31. Cao, W.-T. *et al.* Binary strengthening and toughening of mxene/cellulose nanofiber composite paper with nacre-inspired structure and superior electromagnetic interference shielding properties. *ACS nano* **12**, 4583–4593 (2018).
32. Xu, W. *et al.* Nacre-inspired tunable strain sensor with synergistic interfacial interaction for sign language interpretation. *Nano Energy* **90**, 106606 (2021).
33. Hu, X. *et al.* Nacre-inspired crystallization and elastic “brick-and-mortar” structure for a wearable perovskite solar module. *Energy & Environ. Sci.* **12**, 979–987 (2019).
34. Ma, T. *et al.* A bioinspired interface design for improving the strength and electrical conductivity of graphene-based fibers. *Adv. materials* **30**, 1706435 (2018).
35. Ling, Z. *et al.* Flexible and conductive mxene films and nanocomposites with high capacitance. *Proc. Natl. Acad. Sci.* **111**, 16676–16681 (2014).
36. Wan, S. *et al.* High-strength scalable mxene films through bridging-induced densification. *Science* **374**, 96–99 (2021).
37. Lin, X. *et al.* Fabrication of highly-aligned, conductive, and strong graphene papers using ultralarge graphene oxide sheets. *ACS nano* **6**, 10708–10719 (2012).
38. Lee, G. S. *et al.* Mussel inspired highly aligned $\text{Ti}_3\text{C}_2\text{T}_{x}$ mxene film with synergistic enhancement of mechanical strength and ambient stability. *ACS nano* **14**, 11722–11732 (2020).
39. Ho, J., Jain, A. & Abbeel, P. Denoising diffusion probabilistic models. *Adv. neural information processing systems* **33**, 6840–6851 (2020).
40. Wu, Y. & He, K. Group normalization. In *Proceedings of the European conference on computer vision (ECCV)*, 3–19 (2018).
41. Elfwing, S., Uchibe, E. & Doya, K. Sigmoid-weighted linear units for neural network function approximation in reinforcement learning. *Neural networks* **107**, 3–11 (2018).
42. Perez, E., Strub, F., De Vries, H., Dumoulin, V. & Courville, A. Film: Visual reasoning with a general conditioning layer. In *Proceedings of the AAAI conference on artificial intelligence*, vol. 32 (2018).
43. Woo, S., Park, J., Lee, J.-Y. & Kweon, I. S. Cbam: Convolutional block attention module. In *Proceedings of the European conference on computer vision (ECCV)*, 3–19 (2018).
44. Loshchilov, I. & Hutter, F. Decoupled weight decay regularization. *arXiv preprint arXiv:1711.05101* (2017).